ACS Catalysis
Research Article
pubs.acs.org/acscatalysis

Enhanced Carbon-Resistant Dry Reforming Fe-Ni Catalyst: Role of Fe

Stavros Alexandros Theofanidis, Vladimir V. Galvita,* Hilde Poelman, and Guy B. Marin

Laboratory for Chemical Technology, Ghent University, Technologiepark 914, B-9052 Ghent, Belgium

ABSTRACT: A series of bimetallic Fe-Ni/$MgAl_2O_4$ catalysts with Fe/Ni ratios between 0 and 1.5 have been examined for methane dry reforming at 923−1073 K, atmospheric pressure, and a CH_4/CO_2 ratio of 1. The evolution of the catalyst structure during H_2 temperature-programmed reduction (TPR), CO_2 temperature-programmed oxidation (TPO), and dry reforming is examined using time-resolved in situ X-ray diffraction (XRD). During H_2-TPR up to 973 K, Fe_2O_3 and NiO are reduced to Fe and Ni. Higher temperatures lead to Fe-Ni alloy formation. The alloy remains stable up to 900 K under CO_2-TPO and is decomposed to Ni and Fe_3O_4 at higher temperatures. The Fe-Ni alloy is the active phase while Fe partially segregates from the alloy forming FeO_x during dry reforming. This is beneficial as it reduces the surface carbon accumulation through interaction with FeO_x lattice oxygen, producing CO. Alternate CH_4 and CO_2 pulse experiments over Ni, Fe, and Ni-Fe samples showed that dry reforming over Fe-Ni catalysts can follow a Mars−van Krevelen mechanism. A molar Fe/Ni ratio of 0.7 provides the most active and least deactivated catalyst. All studied catalysts can be regenerated by CO_2 carbon removal.

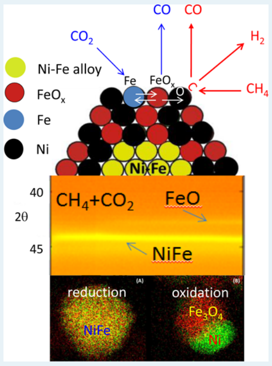

KEYWORDS: *Ni-based catalyst, effect of Fe, alloy, methane dry reforming, synthesis gas, in situ XRD, carbon formation*

1. INTRODUCTION

Methane reforming processes such as steam reforming (SRM), partial oxidation (POM), autothermal reforming (ARM), and dry reforming (DRM) have been investigated intensively.[1] The final H_2/CO product ratio, energetics, and oxidant used differ in these processes.[2] The H_2/CO ratio from DRM is more favorable for Fischer−Tropsch and methanol synthesis in comparison to classical steam reforming. DRM has the lowest operating cost among these processes and offers the additional advantage of converting CO_2 into valuable chemicals:

$$CH_4 + CO_2 \leftrightarrow 2CO + 2H_2 \quad \Delta H^\circ = 261\ \text{kJ mol}^{-1} \tag{1}$$

Side reactions of importance include the water-gas shift:

$$H_2O + CO \leftrightarrow H_2 + CO_2 \quad \Delta H^\circ = -41\ \text{kJ mol}^{-1} \tag{2}$$

However, dry reforming technologies have the disadvantage of rapid catalyst deactivation due to carbon deposition and sintering of both the support and the active metal particles, at high temperatures. The coke originates mainly from two reactions:[3,4]

$$CH_4 \rightarrow C + 2H_2 \quad \Delta H^\circ = 75\ \text{kJ mol}^{-1} \tag{3}$$

$$2CO \leftrightarrow C + CO_2 \quad \Delta H^\circ = -172\ \text{kJ mol}^{-1} \tag{4}$$

Nickel and noble metals such as Pt, Ru, and Rh have been the most investigated catalysts for dry reforming. The aforementioned noble metals show high activity and resistance toward carbon formation.[3−11] Despite their excellent performance, their high cost and limited availability restrict their application in industry. Nickel-based catalysts can offer an alternative, but they are sensitive to deactivation by sintering and carbon encapsulation of Ni under reforming conditions.[12−14] Hence, improvements with respect to both activity and deactivation of Ni catalysts are required. Therefore, much research effort has focused on the effect of supports, promoters, and other metals on Ni-based catalysts.[15−18]

In many cases, Al_2O_3 has been used as a catalyst support.[14,19] In addition, various other support materials such as MgO, ZrO_2, La_2O_3, TiO_2, SiO_2, and SiO_2-Al_2O_3 have been tested.[19−28] There is an agreement in the literature that the mechanism of DRM is strongly dependent on support materials. For catalysts supported on inert materials such as SiO_2,[29] the mechanism follows a monofunctional pathway, where both reactants are activated by the metal alone. Once carbon formation occurs by dehydrogenation of methane, subsequent activation of CO_2 and reaction with carbon are limited, leading to catalyst deactivation. On an acidic[10] (Al_2O_3) or basic[30,31] (La_2O_3, CeO_2, MgO, ...) support, a bifunctional mechanism takes place: CH_4 is activated on the metal, while CO_2 is activated on the support. Zhang and Verykios[30] showed that Ni/La_2O_3 activity increases after 2−5 h of reaction. The studies revealed a large CO_2 pool, stored in the form of $La_2O_2CO_3$. Slagtern and co-workers[32] proposed a bifunctional mechanism for Ni/La_2O_3: methane is activated on the Ni particles and carbon dioxide interacts with La_2O_3, forming carbonates which oxidize carbon deposited on nickel at the Ni−La_2O_3 interface. Ceria is another example of an active support. Bobin and co-workers[33] showed that DRM on metal nanocrystalline doped $CeZrO_2$ oxides demonstrate a high activity and coking resistance by acting as oxygen storage materials. They found that the DRM mechanism on metal nanocrystalline doped $CeZrO_2$ oxides follows a simple redox scheme: CO_2 dissociated on reduced oxide supports while methane reacted

Received: February 17, 2015
Revised: April 3, 2015
Published: April 8, 2015

DOI: 10.1021/acscatal.5b00357
ACS Catal. 2015, 5, 3028−3039

on metal sites. Other than being directly involved in the reactant activation process on its acidic or basic sites, the supports also affect the metal particle size or metal dispersion. Suitable supports have to be resistant to high temperature and should be able to maintain the metal dispersion during operation.

Suitable supports have to be resistant to high temperature and should be able to maintain the metal dispersion during operation.[34] The addition of MgO to Al_2O_3 prevents the interaction between active metals (Ni and Fe) and the alumina-forming $NiAl_2O_4$ and $FeAl_2O_4$ spinel phases that are inactive.[12] Guo and co-workers[34] compared Ni/γ-Al_2O_3, Ni/MgO-γ-Al_2O_3, and Ni/$MgAl_2O_4$ during methane dry reforming. They found that Ni/$MgAl_2O_4$ exhibits higher activity and better stability in comparison to the other samples. The $MgAl_2O_4$ spinel can effectively suppress the phase transformation to form $NiAl_2O_4$ and can stabilize Ni crystallites. Penkova and co-workers[35] found that incorporating a basic element (Mg) into the alumina support alters the surface structure, leading to a modification of the acid−base properties of the support. The resulting magnesium aluminate spinel ($MgAl_2O_4$) combines desirable properties for use in ceramics, due to its high melting temperature (2408 K), mechanical strength, and good chemical stability.[34] Hence, in this work $MgAl_2O_4$ is examined as a Ni support because of its low acidity, compared to Al_2O_3, and sintering resistance due to strong interaction of metal oxides with $MgAl_2O_4$, resulting in high metal dispersion after reduction.[36−38]

The accumulation of carbon on the catalyst surface depends on the oxidation rate of dehydrogenated CH_x species, originating from CH_4 decomposition, and thus on the surface oxygen species availability. In view of increasing the available O species, the addition of oxides to Ni has been examined. A possible oxide is CeO_2, because it is known for its ability to easily release oxygen and quickly reoxidize in the presence of oxidative agents.[33,39] CeO_2 indeed enhances the catalytic performance by forming a Ni-CeO_2 nanocomposite.[39] The good catalytic activity and high resistance toward carbon formation were assigned to the large interface between metallic Ni and the CeO_2 surface and to the metal−ceria interactions which strongly affect their redox and catalytic properties.[40]

An additional way of improving catalytic performance is by alloy formation between Ni and other metals.[41,42] It has been reported that the addition of noble metals (Ru, Rh, Pd, Pt) to Ni-based catalysts results in alloy formation after reduction, improving the catalyst activity and stability.[43−46] Apart from noble metals, a synergistic effect of alloy formation between Ni and Co has been reported in tar steam reforming.[47] In this respect, Fe_2O_3 can also make a suitable promoter, as it combines good redox properties, like CeO_2, with Fe-Ni alloy formation upon intimate interaction between Fe and Ni. An improved performance in the steam reforming activity of Ni-Fe/Al_2O_3 was attributed to the formation of a Ni-Fe alloy so that Fe acts as a cocatalyst.[42] Moreover, under industrial CO methanation reaction conditions, Ni-Fe bimetallic catalysts on γ-Al_2O_3 exhibited higher catalytic activity than the monometallic catalysts.[48] These results make iron oxide an interesting material for improvement of the Ni/$MgAl_2O_4$ activity and resistance toward carbon deposition. Ashok and Kawi studied toluene steam reforming over a Ni/Fe_2O_3-Al_2O_3 catalyst, examining the effect of iron−alumina calcination temperature on steam reforming.[14] They found that Ni−Fe alloys were formed and remained stable throughout the reforming reaction.

In order to further evaluate the effect of Fe on Ni/$MgAl_2O_4$, a series of Fe-Ni/$MgAl_2O_4$ samples for use in methane dry reforming is investigated in this work. One aspect that awaits clarification is whether and how the Ni−Fe alloy contributes to the elimination of carbon deposition during the dry reforming reaction. In addition, the mechanism for dry reforming over a Fe-Ni catalyst is not clear. These questions have been addressed by performing in situ X-ray diffraction (XRD) characterization of Fe-Ni/$MgAl_2O_4$ catalysts during temperature-programmed reduction (TPR), oxidation, and dry reforming. Alternate pulse experiments are also applied by switching the flow between CO_2 and CH_4 over Ni/$MgAl_2O_4$, Fe/$MgAl_2O_4$, and Fe-Ni/$MgAl_2O_4$.

2. EXPERIMENTAL METHODS

2.1. Catalyst Preparation.

2.1.1. Support Preparation. $MgAl_2O_4$ support material was prepared by coprecipitation from an aqueous solution of $Mg(NO_3)_2{\cdot}6H_2O$ (99%, Sigma-Aldrich) and $Al(NO_3)_3{\cdot}9H_2O$ (98.5%, Sigma-Aldrich) (molar ratio Mg/Al = 1/2). A precipitating agent, NH_4OH (ACS reagent, 28.0−30.0% NH_3 basis), was added to adjust the pH to 10, at 333 K. The produced precipitate was filtered, dried at 393 K for 12 h, and subsequently calcined in air at 1023 K for 4 h.

2.1.2. Catalyst Preparation. Four Fe-Ni catalysts were prepared by incipient wetness impregnation on the support ($MgAl_2O_4$) using an aqueous solution of corresponding nitrates $Ni(NO_3)_2{\cdot}6H_2O$ (99.99+%, Sigma-Aldrich) and $Fe(NO_3)_3{\cdot}9H_2O$ (99.99+%, Sigma-Aldrich).[49] The catalysts were dried at 393 K for 12 h and subsequently calcined in air at 1023 K for 4 h. The Fe/Ni molar ratios were 0, 0.7, 1.1, and 1.6. Samples are labeled using their molar ratio *X* as *X*-Fe/Ni, as shown in Table 1. In addition, a 5 wt % Fe sample was synthesized on the same support for comparison purposes.

2.2. Catalyst Characterization.

The Brunauer−Emmett−Teller (BET) surface area of each sample was determined by N_2 adsorption at 77 K (five-point BET method using Gemini Micromeritics) after outgassing the sample at 473 K for 2 h. The crystallographic phases of the materials as prepared were confirmed by ex situ XRD measurements (Siemens diffractometer Kristalloflex D500, Cu Kα radiation). The powder patterns were collected in a 2θ range from 10 to 80° with a step of 0.02° and 30 s counting time per angle. XRD patterns of known compounds are referenced by their corresponding number in the Powder Diffraction File database. By fitting of a Gaussian function to a diffraction peak, the crystallite size was determined from the peak width via the Scherrer equation,[50] while the peak position gives information about the lattice spacing on the basis of the Bragg law of diffraction.[51]

The bulk chemical compositions of support and as-prepared catalysts were determined by means of inductively coupled plasma atomic emission spectroscopy (ICP-AES, ICAP 6500, Thermo Scientific). The samples were mineralized by alkaline fusion with a mix of Li-tetraborate and Li-metaborate.

Scanning electron microscopy (SEM; FEI Quanta 200F) was performed to evaluate the surface morphology of the materials. An acceleration voltage of 25 or 12.5 kV was chosen for the secondary electron SEM images. Energy-dispersive X-ray (EDX) spectroscopy (EDAX Inc.) at 17.5 kV acceleration voltage provided a first compositional analysis, typically in a 1 μm thick volume.

High-resolution transmission electron microscopy (HRTEM) was used for structural analysis, while EDX yielded local chemical analysis. These techniques were implemented

DOI: 10.1021/acscatal.5b00357
ACS Catal. 2015, 5, 3028−3039

using a JEOL JEM-2200FS Cs-corrected microscope operated at 200 kV, which was equipped with a Schottky-type field-emission gun (FEG) and EDX JEOL JED-2300D instrument. All samples were deposited by immersion onto a lacey carbon film on a copper support grid.

2.3. In Situ Time-Resolved XRD. In situ XRD measurements were performed in a home-built reaction chamber housed inside a Bruker-AXS D8 Discover apparatus (Cu Kα radiation of 0.154 nm). The reactor chamber had a Kapton foil window for X-ray transmission. The setup was equipped with a linear detector covering a range of 20° in 2θ with an angular resolution of 0.1°. The pattern acquisition time was approximately 10 s. All temperatures were measured with a K-type thermocouple and corrected afterward to a calibration curve of the heating device, which is based on the eutectic systems Au−Si, Al−Si, and Ag−Si. For each sample, approximately 10 mg of powdered sample was evenly spread on a single-crystal Si wafer. Interaction of the catalyst material with the Si wafer was never observed. Before each TPR/TPO experiment, the reactor chamber was evacuated to a base pressure of 4 Pa by a rotation pump. Gases were supplied to the reactor chamber from a rig with calibrated mass-flow meters. He (1 mL/s) was flowing for 15 min before the flow switched to 1 mL/s of 10% H_2/He or CO_2 for TPR and TPO, respectively.

The evolution of the catalyst structure during the TPR, TPO, and DRM reaction was investigated. For TPR and TPO experiments, the sample was heated from room temperature to 1123 K at a heating rate of 30 K/min in a flowing gas stream (1 mL/s of 10% H_2/He or CO_2, respectively). For DRM reaction experiments the sample was first reduced (1 mL/s of 10% H_2/He) at 1123 K, while the reaction temperature was 973 K. A full XRD scan (10−65° with a step of 0.02°) was taken at room temperature before and after each TPR, TPO, and DRM reaction experiment. Samples were cooled in a helium flow to room temperature after each experiment.

It should be noted that the peaks in the in situ XRD patterns appeared at slightly shifted angular positions in comparison to both full scans and tabulated values due to temperature-induced lattice expansion and different sample heights. These shifts in peak positions, which are not related to underlying physicochemical processes, were taken into account during peak assignment.

2.4. Catalytic Activity. Activity measurements were performed at atmospheric pressure in a quartz U-tube reactor with an internal diameter of 10 mm, which was housed inside an electric furnace (AutoChem II 2920 Micromeritics equipped with a TCD detector). A 10−20 mg portion of the sample with particle size of ~30 μm, diluted with inert Al_2O_3 (catalyst/inert ratio 1/60), was packed between quartz wool plugs. The temperature of the catalyst bed was measured with K-type thermocouples touching the outside and inside of the reactor at the position of the catalyst bed. The inlet gas flow rates were always maintained by means of calibrated Brooks mass flow controllers. The outlet gas stream was monitored online using a calibrated OmniStar Pfeiffer mass spectrometer (MS). MS signals were recorded for all major fragments. For quantification of each component, the MS was focused to different signals (amu), the selection of which was based on the analysis of the mass spectra of the individual components. H_2 was monitored at 2, He at 4, CH_4 at 16, H_2O at 18, CO at 28, Ar at 40, and CO_2 at 44. When there was an unavoidable interference with fragmentation peaks of other gases, a correction was applied to remove their contributions: e.g., CO was monitored at 28 amu, subtracting the contribution of CO_2, i.e., not more than 10% of the peak at 28 amu. A carbon balance with a maximum deviation of 5% was obtained. Dimensionless criteria were applied for evaluating the significance of external and internal heat and mass transfer limitations. The absence of external and internal mass transfer limitations was verified using the Carberry number[52] and Weisz−Prater criterion,[53] while for heat transport limitations the diagnostic criteria reported by Mears[54] were applied.

The activity was measured from 823 to 1073 K. First the sample was reduced in a 1 mL/s flow of 5% H_2/Ar at 1123 K for 30 min and then the flow was switched to He for 10 min. After this step a mixture of 50% CH_4−50% Ar and CO_2 (volume ratio 2/1, volume ratio CH_4/CO_2 = 1/1, internal standard Ar) started flowing inside the reactor for the methane dry reforming reaction. Produced CO and H_2 and unconverted CH_4 and CO_2 were detected at the outlet. For each catalyst sample, the activity was measured at five different temperatures. At each temperature the reaction took place for 6 min, when the rate of CH_4 and CO_2 consumption was stable.

The activity was also measured as a function of time on stream. The experiment was carried out at the same temperature, pressure, dilution ratio between catalyst and inert, flow rates of reactants (CH_4/CO_2 1/1), and conversion. The same conversion (X_{CH_4} = 51%) for all of the investigated samples was achieved by varying the amount of catalyst.

The following expressions are used to determine the activity of different catalysts. The percent conversion for a reactant is calculated as

$$X_i = \frac{F_{i,0} - F_i}{F_{i,0}}. \tag{5}$$

where $mol_{i,0}$ and mol_i are the inlet and outlet moles of reactant i.

The site-time yield (STY, $mol\cdot s^{-1}\cdot mol^{-1}{}_{Ni}$) was calculated from the difference in the inlet and outlet molar flow rates, as measured relative to an internal standard (Ar).

$$STY_i = |(F_{in,i} - F_{out,i})|/N_{Ni} \tag{6}$$

where F_i (mol s^{-1}) is the molar flow rate of component i and N_{Ni} (mol_{Ni}) is the number of exposed, i.e. surface, Ni atoms in the reaction. The fraction of exposed Ni atoms was calculated under the assumption that it was determined by the most abundant crystallite phase.

Regeneration cycles were performed combining periods of methane dry reforming with periods of catalyst oxidation with CO_2 for carbon removal and finally reduction for alloy formation.[55] Burning carbon by oxygen or air is a strongly exothermic reaction and hence would lead to catalyst bed temperature increase. In each methane dry reforming period, the methane STY was calculated after TOS = 30 min. The standard error was calculated out of three independent experiments.

Carbon formation over the studied catalysts was investigated using methane decomposition, considering that this is the main source of carbon formation at 1023 K. The reaction took place in a quartz tube reactor at 1023 K for 6 min. The inlet 50% CH_4−50% Ar gas flow rate was 1 mL/s. The deposited carbon was then oxidized by CO_2, while the produced CO and unconverted CO_2 were detected in the outlet. Then the flow

Table 1. Catalyst and Support Properties

abbreviation	catalyst	Fe/Ni (mol/mol)	metal loading (wt %)		BET (m^2/g_{cat})	metal fraction exposed[a] (%)	crystallite size of active phase Ni and Fe-Ni alloy (nm)[b]
			Ni	Fe			
MgAl	$MgAl_2O_4$				100.3 ± 15.2		
0-Fe/Ni	8 wt % $Ni/MgAl_2O_4$	0	7.85		81.9 ± 9.8	9.5	10.5
0.7-Fe/Ni	8 wt % Ni−5 wt % $Fe/MgAl_2O_4$	0.7	7.50	4.95	84.7 ± 5.8	7.0	14.3
1.1-Fe/Ni	8 wt % Ni−8 wt % $Fe/MgAl_2O_4$	1.1	7.20	7.30	47.6 ± 11.4	7.5	13.4
1.6-Fe/Ni	8 wt % Ni−11 wt % $Fe/MgAl_2O_4$	1.6	7.20	10.90	68.4 ± 6.7	5.1	19.5

[a] The fraction of exposed Ni sites was calculated as $(1/d_{Ni}) \times 100$, where d_{Ni} is the crystallite diameter in nm. [b] The crystallite sizes of Ni and Fe-Ni alloy were calculated from full scan XRD patterns obtained after H_2 reduction.

was switched to O_2 in order to burn the remaining carbon, if any.

2.5. Alternate Pulse Experiment. An isothermal pulse experiment was performed using a quartz tube reactor at 1023 K. The reactor was filled with catalyst and inert alumina as diluent, in a 1/60 ratio. As a first step, a pulse of CO_2 was admitted over 1 min, while the CO production was monitored by online MS. Then, He started to flow inside the reactor in order to remove the remaining CO_2. As a final step, a CH_4 pulse followed for 1 min under the same conditions, with monitoring of the CO production. The 5% $Fe/MgAl_2O_4$ sample was also tested during an alternate pulse experiment.

3. RESULTS AND DISCUSSION

3.1. Catalyst Characterization. The Brunauer−Emmett−Teller (BET) surface area, metal content, and average diameter of Ni crystallites are reported in Table 1 for the samples used in this study. The supported Ni-based catalysts have lower surface areas than the bare support. This is mainly due to pore blockage.[14] The surface area of the support and the pure Ni supported sample were above previously reported values.[4,34,56] It was observed that the BET surface area decreases as the metal content increases, but it remains stable for the last two samples (1.1Fe/Ni and 1.6Fe/Ni). The crystallite sizes calculated from XRD are in line with the average particle sizes as observed in HRTEM.

The crystalline phases of as-prepared, reduced, and reoxidized catalysts were confirmed by ex situ powder XRD. Figure 1A shows examples of pure support, as-prepared, and reduced Fe-promoted samples (0.7-Fe/Ni), while Figure 1B illustrates the full scan XRD patterns of 0.7-Fe/Ni after CO_2 oxidation. $MgAl_2O_4$ (31.7, 37, 45, 55.5, 59, and 65°, Powder Diffraction File (PDF) card number 00-021-1152) remained stable during reduction and oxidation for all samples (full scan XRD patterns for the other studied samples are not shown). Fe_2O_3 (maghemite), NiO, and $NiAl_2O_4$ peaks (30.2, 35.6, 43.3, 57.3, and 62.9°, PDF 00-039-1346; 37.3, 43.3, and 62.9°, PDF 01-089-5881; 37.0, 45, 59.7, and 65.5°, PDF 00-010-0339), some of which are overlapping, were observed for the as-prepared sample. It cannot be excluded that the peaks (30.2, 35.6, 43.3, 57.3, and 62.9°) correspond to $NiFe_2O_4$ instead of Fe_2O_3, as they cannot be distinguished due to overlapping. Upon reduction, NiO and Fe_2O_3 diffractions disappeared, while NiO completely integrated in the spinel structure to form $NiAl_2O_4$ was not reduced. This is in accordance with Guo and co-workers,[34] who also observed the formation of an $NiAl_2O_4$ crystalline phase. In addition, diffractions are present at angles lower than that of metallic Ni. The shift is attributed to formation of a Fe-Ni alloy (44 and 51.5°), and this was also observed in previous reports.[14,42] According to the Fe-Ni phase diagram[57] at least one regular Ni-rich alloy with Ni_3Fe composition is known. Other Fe-Ni alloy structures with compositions NiFe, Ni_3Fe_2, and Ni_2Fe have been also reported.[56] The XRD pattern following the CO_2-TPO (Figure 1B) shows that Fe-Ni alloy was decomposed to Ni (44.5°) and Fe_3O_4 (30.1, 36, 43.5, 57, and 63°), while the $NiAl_2O_4$ and $MgAl_2O_4$ substrate diffractions remained stable. For 1.1-Fe/Ni and 1.6-Fe/Ni, the XRD patterns showed an extra peak, after H_2-TPR, originating from metallic Fe (45°) which was not engaged in alloy formation (not shown).

The elemental distribution of 0.7-Fe/Ni is indicated in Figure 2 using energy-dispersive X-ray spectroscopy (EDX)-STEM mapping. Both Fe (red) and Ni (green) elements were distributed uniformly in the sample after reduction, implying the alloy formation. In contrast, after CO_2 oxidation Ni and Fe particles were segregated as Fe was oxidized to Fe_3O_4 and the Fe-Ni alloy was decomposed.

3.2. In Situ XRD Time-Resolved Measurements. *3.2.1. H_2-TPR.* The Fe-Ni alloy formation during the H_2-TPR process was investigated using in situ XRD measurements for all studied samples. The results for the 0.7-Fe/Ni sample are presented in Figure 3A. Diffraction peaks associated with Fe_2O_3 were not detected by in situ XRD due to the low concentration and overlapping with $MgAl_2O_4$ peaks. During reduction, NiO peaks disappear above 973 K. The Ni-related diffraction shifts to an angle of 44°, lower than that for metallic Ni, which hence corresponds to a Fe-Ni alloy peak.[14,42,58,59] The kinetics of NiO reduction and alloy formation are depicted in Figure 3B as integral intensity variation of the diffraction peaks with temperature. At 973 K the intensity in the angle region 43.7−44.2° increases because of the appearance of the Fe-Ni alloy diffraction.

The intensity of characteristic peaks associated with crystalline MgAl did not change throughout H_2-TPR until the final temperature of 1123 K, implying that MgAl was not reduced in this temperature range. The small shift of angular positions in comparison to full scan XRD patterns at room temperature can be ascribed to temperature-induced lattice expansion and different sample height.

3.2.2. CO_2-TPO. To test the stability of the Fe-Ni alloy in the presence of CO_2, CO_2-TPO was performed immediately after cooldown following H_2-TPR (Figure 4A). The oxidation reaction of the Fe-Ni alloy in 0.7-Fe/Ni resulted in alloy decomposition above 900 K into Ni and Fe_3O_4. The

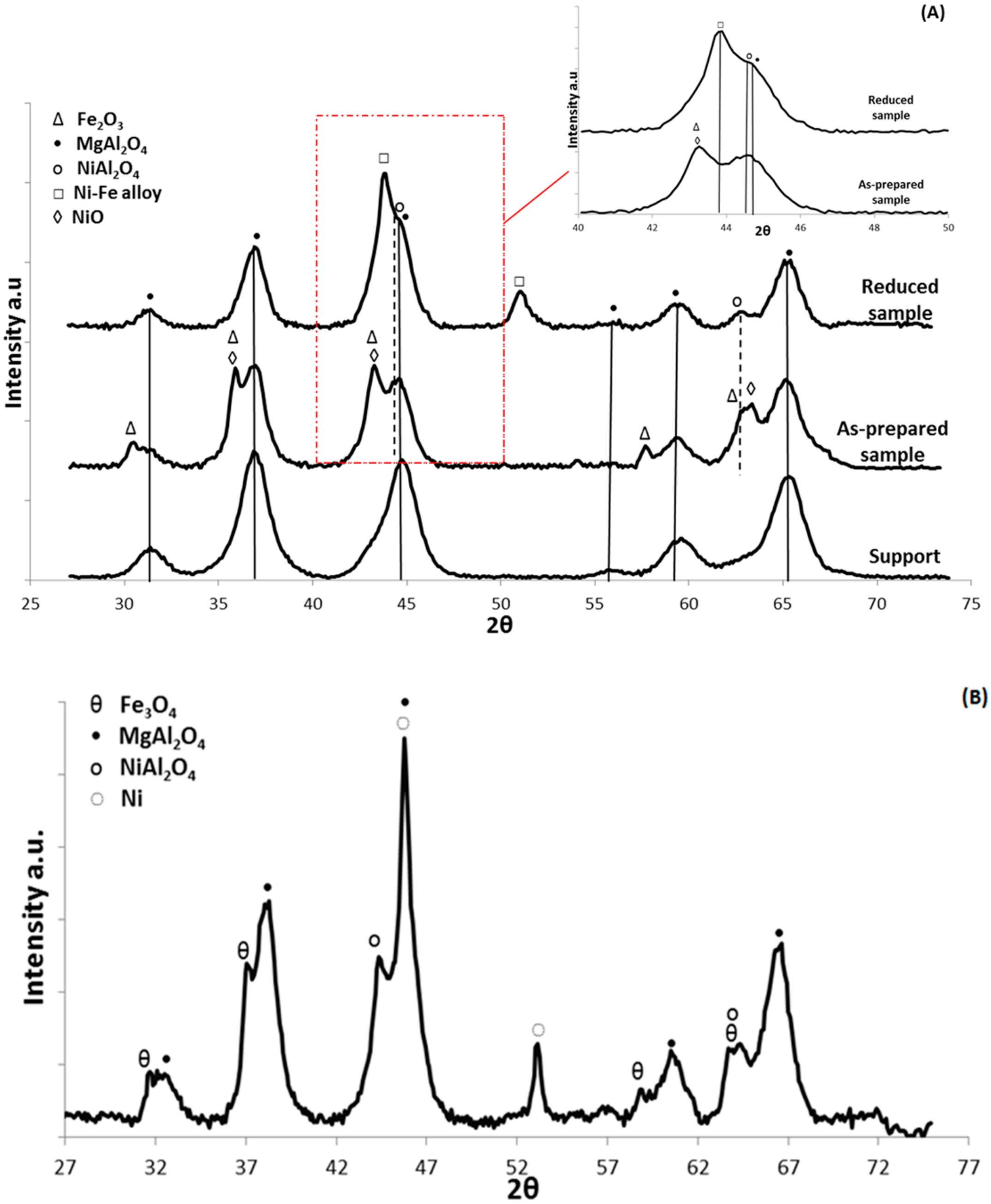

Figure 1. Full XRD scans of (A) $MgAl_2O_4$ and as-prepared and reduced 0.7-Fe/Ni (1 mL/s of 10% H_2/He mixture at a total pressure of 101.3 kPa and 1123 K). The upper right inset shows the highlighted rectangular area at higher resolution. (B) 0.7-Fe/Ni after CO_2 oxidation (1 mL/s of CO_2, at a total pressure of 101.3 kPa and 1123 K).

intermediate phase of FeO was not observed. It has been reported that the formation of FeO strongly depends on reaction temperature and gas composition.[60] Further oxidation of Fe_3O_4 to Fe_2O_3 cannot be achieved by applying gaseous CO_2. The kinetics of the alloy decomposition are illustrated in Figure 4B as time-dependent integral intensities of the Fe-Ni alloy and Fe_3O_4 angular regions. The Ni peak intensity is not depicted because of overlap with a $MgAl_2O_4$ peak.

A graphical illustration of the Fe-Ni alloy formation and decomposition is depicted in Figure 5. The alloy was decomposed during CO_2 oxidation between 850 and 1123 K, yielding two separate phases of Ni and Fe_3O_4 (see EDX elemental mapping image in Figure 2). Metallic Ni remained stable under a CO_2 flow and was not oxidized to NiO. A subsequent H_2 reduction step led again to Fe-Ni alloy formation for all of the studied samples (not shown).

3.3. Activity Tests. The effect of Fe-Ni alloying on the catalytic properties of Fe-Ni/$MgAl_2O_4$ was examined by a set of activity measurements under methane dry reforming reaction conditions. Figure 6 shows the variation of STY_{CH_4}/STY_{CO_2} with temperature. Each temperature was maintained for 6 min until the measured temperature inside the catalyst bed was stable. STY_{CH_4}/STY_{CO_2} was above unity for almost all catalyst samples, implying that in the first few minutes of the reaction the CH_4 consumption was higher than that of CO_2. On the basis of DRM and reverse water-gas shift (RWGS) reactions, it was expected that STY_{CH_4}/STY_{CO_2} would remain below 1.

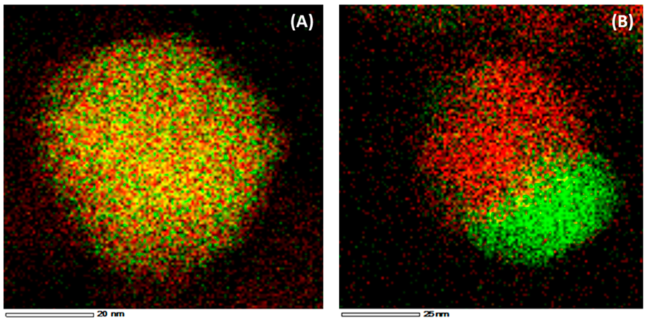

Figure 2. EDX element mapping of 0.7-Fe/Ni: (A) after H_2 reduction (1 mL/s of 5% H_2/Ar mixture at a total pressure of 101.3 kPa and 1123 K); (B) after CO_2 oxidation (1 mL/s of CO_2 at a total pressure of 101.3 kPa and 1123 K). Red and green colors correspond to Fe and Ni elements, respectively.

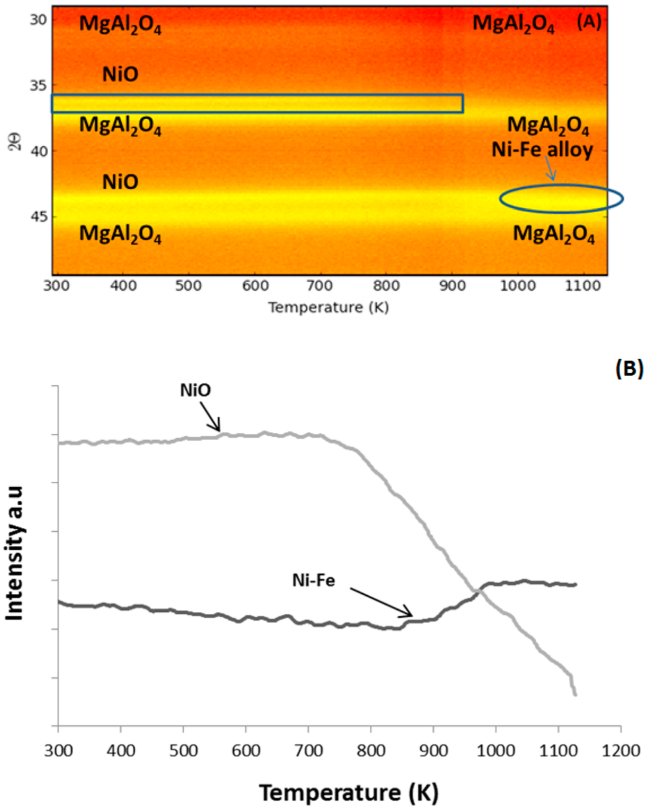

Figure 3. In situ XRD during H_2-TPR: (A) 2D XRD pattern for 0.7-Fe/Ni (heating rate 30 K/min, maximum temperature 1123 K, flow rate 1 mL/s, 10% H_2/He); (B) integral intensity variation of (A) for diffraction areas 35.5−36.5° (NiO) and 43.7−44.2° (Fe-Ni alloy).

There are two relative rates that contribute to the STY_{CH_4}/STY_{CO_2} ratio. The first depends on the methane decomposition rate to surface carbon and H_2 (eq 3) . The second depends on surface carbon oxidation by oxygen which is derived from CO_2, at the applied operating temperature and reactant partial pressure. Initially the rate of methane decomposition is higher than that of surface carbon oxidation, but it decreased after 10−15 min, due to deactivation of Ni surface sites, which are more active for methane cracking.[61,62] This was ascribed to a lower CO_2 consumption, in comparison to Fe-promoted samples, as the methane conversion was the same for all of the studied catalysts.

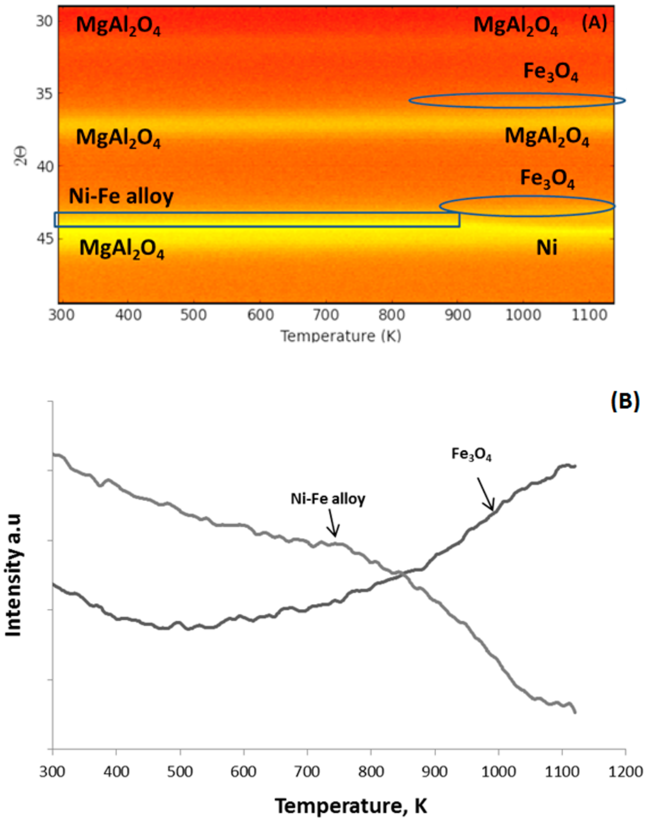

Figure 4. In situ XRD during CO_2-TPO: (A) 2D XRD pattern for 0.7-Fe/Ni (heating rate 30 K/min, maximum temperature 1123 K, flow rate 1 mL/s, 100% CO_2); (B) integral intensity variation of (A) for diffraction areas 35.4−36.4° (Fe_3O_4) and 43.7−44.2° (Fe-Ni alloy).

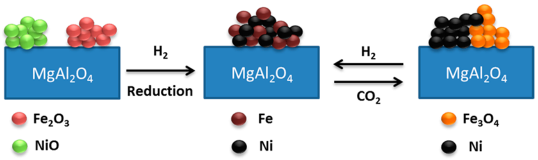

Figure 5. Schematic diagram of Fe-Ni alloy formation, during H_2-reduction, and decomposition, during CO_2 oxidation.

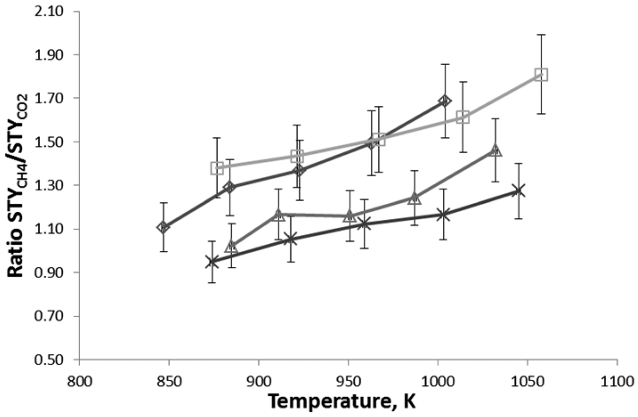

Figure 6. STY_{CH_4}/STY_{CO_2} ratio as a function of temperature for methane dry reforming (6 min at each temperature, W_{cat}/F_{CH_4} = 0.40−0.71 kg_{cat} s mol^{-1}): (◇) 0-Fe/Ni; (□) 0.7-Fe/Ni; (△) 1.1-Fe/Ni; (×) 1.6-Fe/Ni.

Figure 7 illustrates the dependence of STY_{CH_4}/STY_{CO_2} on time-on-stream during isothermal dry reforming at 1023 K for all catalysts. 0-Fe/Ni showed the highest STY_{CH_4}/STY_{CO_2} ratio.

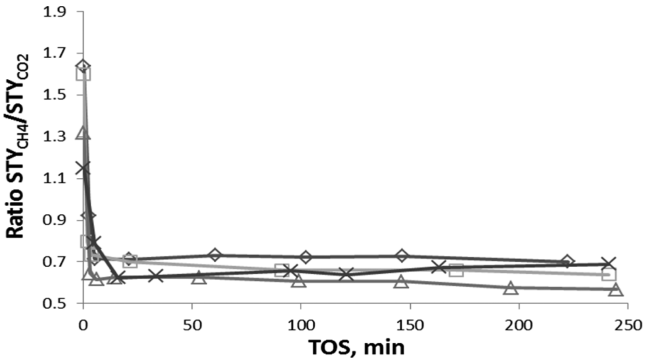

Figure 7. STY_{CH_4}/STY_{CO_2} ratio with time-on-stream (TOS, min) for methane dry reforming at 1023 K (W_{cat}/F_{CH_4} = 0.40−0.71 kg_{cat} s mol^{-1}, CH_4/CO_2 = 1/1, total pressure of 101.3 kPa): (◇) 0-Fe/Ni; (□) 0.7-Fe/Ni; (△) 1.1-Fe/Ni; (×) 1.6-Fe/Ni.

The addition of Fe increases the CO_2 conversion. This means that CO_2 selectively reacts with methane or that CO_2 is consumed according to the water-gas shift reaction (eq 2).

The CO and H_2 STY results of a series of isothermal activity measurements in a fixed bed reactor are depicted in Figure 8 (0-Fe/Ni and 0.7-Fe/Ni are shown). CO production was higher for all Fe-promoted samples than for 0-Fe/Ni. Specifically, the 0.7-Fe/Ni catalyst showed a higher CO production and the CO/H_2 ratio was close to unity (Figure 9), making it suitable for the Fischer−Tropsch process and methanol synthesis.

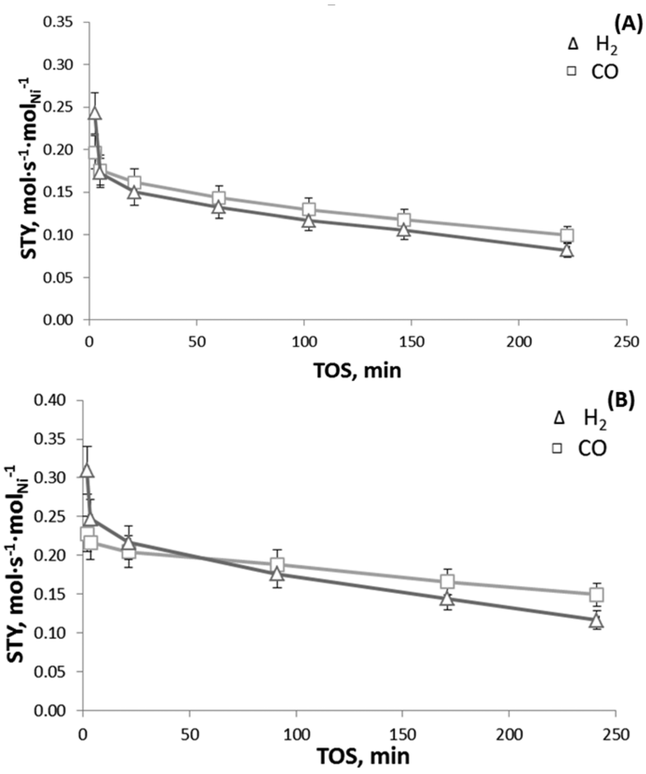

Figure 8. Site time yield for H_2 and CO (STY, mol s^{-1} $mol_{Ni}{}^{-1}$) with time-on-stream (TOS, min) for methane dry reforming at 1023 K (W_{cat}/F_{CH_4} = 0.40−0.71 kg_{cat} s mol^{-1}, CH_4/CO_2 = 1/1, total pressure of 101.3 kPa): (A) 0-Fe/Ni; (B) 0.7-Fe/Ni.

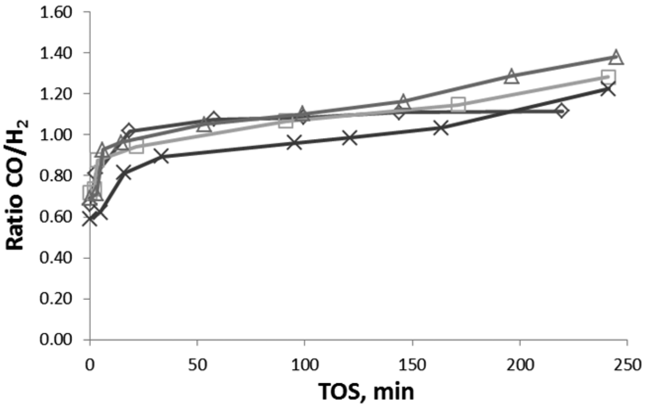

Figure 9. CO/H_2 ratio with time-on-stream (min) for all studied catalysts. (◇) 0-Fe/Ni; (□) 0.7-Fe/Ni; (△) 1.1-Fe/Ni; (×) 1.6-Fe/Ni (error bars not shown).

It is also observed that 0.7-Fe/Ni has an optimal composition, as it results in higher CO and H_2 production and less deactivaion, from 0.23 to 0.15 mol_{CO} s^{-1} $mol_{Ni}{}^{-1}$ and from 0.31 to 0.12 mol_{H_2} s^{-1} $mol_{Ni}{}^{-1}$. The addition of Fe promotes methane dry reforming in the molar ratio range Fe/Ni $\leq$ 0.7. More Fe addition results in catalyst activity decrease. These results are in accordance with Wang and co-workers,[42] who found that the addition of Fe can have either a promoting or a suppressing effect on catalytic steam reforming of tars.

Carbon formation on Fe-promoted and nonpromoted samples was compared by SEM micrographs and EDX analysis of spent catalysts. Figure 10A shows carbon filaments grown on 0-Fe/Ni[63] after 4 h on-the-stream under methane dry reforming at 1023 K. The corresponding EDX spectrum (see Figure 10B) confirms the high concentration of carbon in this sample. On the other hand, a negligible amount of carbon was deposited on 1.1-Fe/Ni (Figure 10C) as can be verified by the respective EDX spectrum (see Figure 10D).

The high amount of carbon deposited on used 0-Fe/Ni agrees with the higher STY_{CH_4}/STY_{CO_2} ratio in comparison to that for Fe-promoted samples (see Figure 7), observed during methane dry reforming.[14,42] A higher STY_{CH_4}/STY_{CO_2} ratio means more CH_4 was converted than CO_2 and as a result more carbon is formed (Figure 10). Fe addition increases CO_2 conversion but also suppresses carbon deposition.

3.4. Regeneration Cycles. As seen in Figure 8, the activity of the studied catalysts decreases with time-on-stream. To evaluate the catalyst regeneration ability, three catalytic cycles were performed that combined periods of methane dry reforming with periods of catalyst oxidation with CO_2 for carbon removal and finally reduction for alloy formation. In each DRM period, the methane STY was calculated after TOS = 30 min (Figure 11). The duration of the DRM in the first cycle was 4 h, while the duration in the second and third cycles was reduced to 1 h. The CO_2 oxidation step was always 20 min at 1023 K, and the subsequent H_2 reduction step was also 20 min at 1123 K.

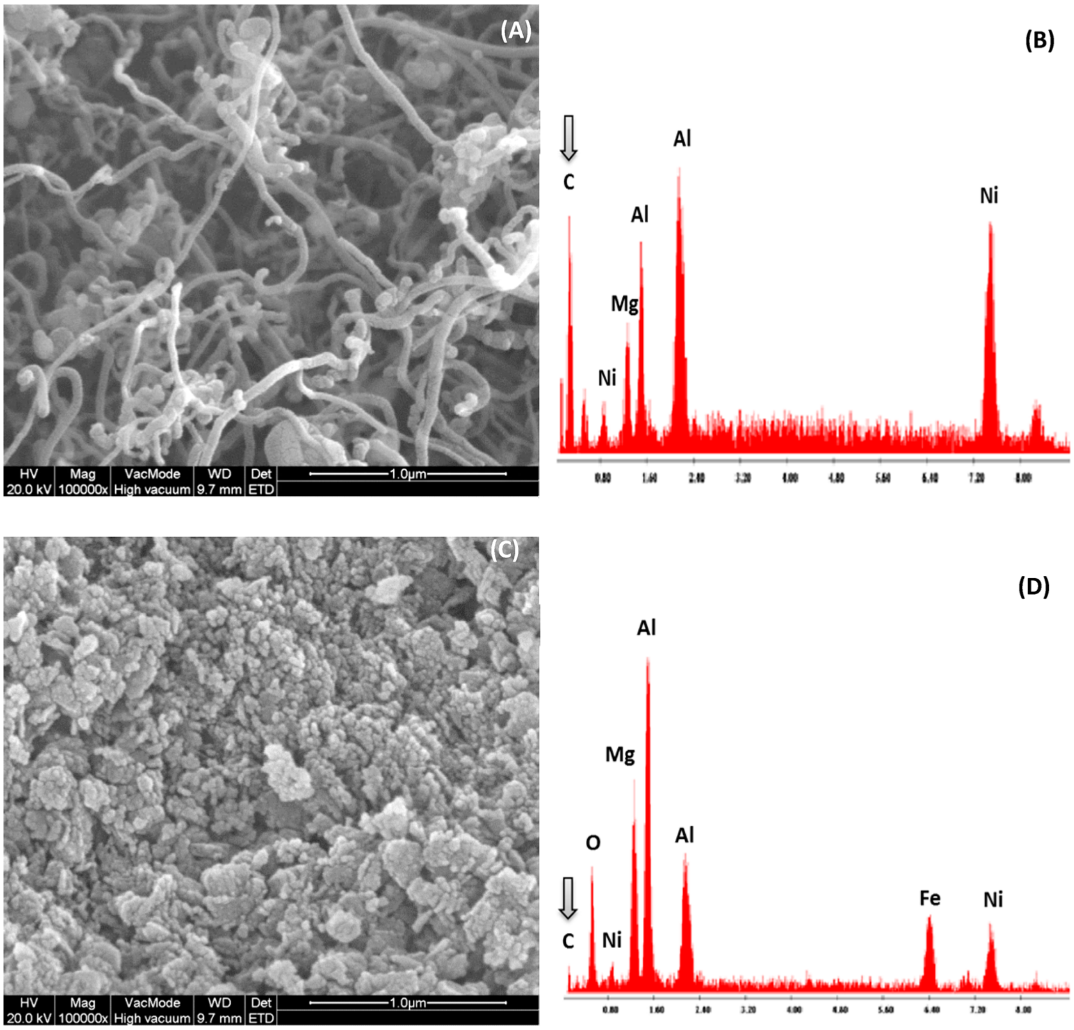

Figure 10. SEM micrographs and EDX analysis of spent catalysts (temperature 1023 K, CH_4/CO_2 = 1/1, reaction time 4 h): (A) 0-Fe/Ni SEM image; (B) 0-Fe/Ni EDX; (C) 1.1-Fe/Ni SEM image; (D) 1.1-Fe/Ni EDX.

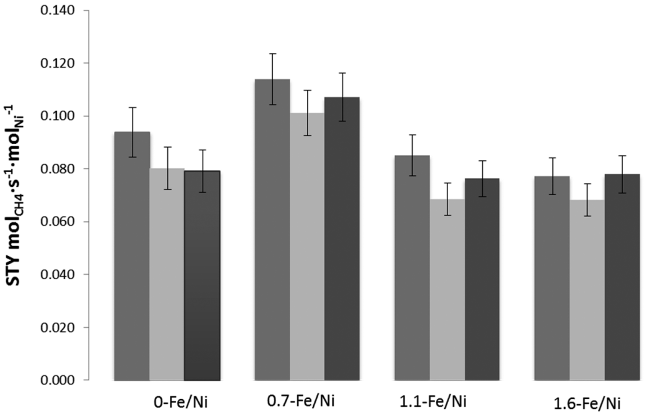

Figure 11. Methane site time yield (STY, $mol_{CH_4}\ mol_{Ni}^{-1}\ s^{-1}$) during three catalytic cycles: first cycle DRM, TOS = 4 h; second and third cycle DRM, TOS = 1 h. CO_2 oxidation and H_2 reduction: each 20 min. The STY for each cycle was calculated after TOS = 30 min.

Figure 11 shows that all catalysts can be regenerated. The pure Ni sample remains at a slightly lower level of activity even after the second regeneration (STY in the third cycle). The Fe-promoted samples restore higher activity after the second regeneration than after the first. For the highest Fe loading, 1.6-Fe/Ni, the initial activity is even completely recovered after two regeneration cycles.[55] Furthermore, a higher amount of carbon was deposited on 0-Fe/Ni (244.6 $mol_C\ mol_{Ni+Fe}^{-1}$) than on Fe-promoted samples (5.6, 0.9, and 0.7 $mol_C\ mol_{Ni+Fe}^{-1}$ for 0.7-Fe/Ni, 1.1-Fe/Ni, and 1.6-Fe/Ni, respectively) during DRM of the first cycle. This is in agreement with the SEM-EDX characterization of spent catalysts (parts A–D of Figure 10), where more carbon deposition was observed on 0-Fe/Ni than on the Fe-promoted sample.

3.5. Effect of Alloy on Carbon Formation. The contribution of the alloy formation to the elimination of carbon deposition was investigated under methane decomposition reaction conditions (see section 2.4). The carbon that accumulated according to eq 3[64] was subsequently oxidized by CO_2 according to the Boudouard reaction (eq 4). In order to examine whether the filamentous carbon that formed actually interacted with CO_2 to be burnt, the flow was switched afterward to O_2 to burn off any remaining carbon. All deposited carbon was removed, however, during CO_2 oxidation, as no CO production was observed during subsequent O_2 oxidation.

Figure 12 illustrates the produced CO by CO_2 oxidation of deposited carbon. The area under each curve corresponds to the produced moles of CO, and this value was normalized per mole of metal loading (Ni and Fe). The 1.1-Fe/Ni sample

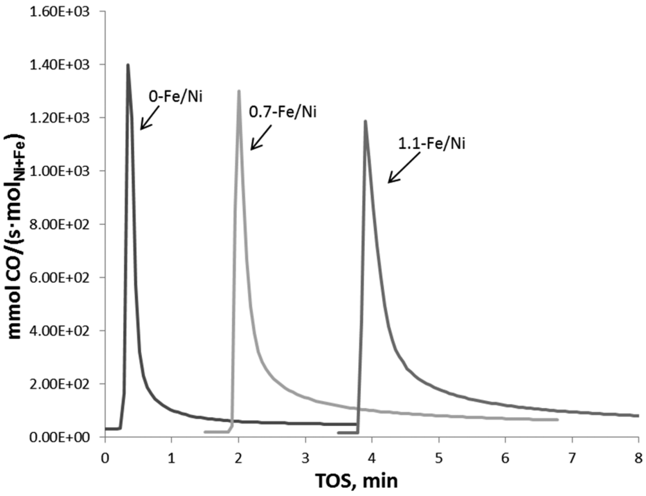

Figure 12. CO site time yield (STY, mol$_{CO}$ mol$_{Ni+Fe}^{-1}$ s^{-1}) upon CO_2 oxidation of deposited carbon for different catalysts. The carbon was formed after pulsing methane for 6 min at 1023 K for all prereduced samples (1123 K, 1 mL/s 5% H_2/He). Total amount of CO produced: (1) 2.47 mol$_{CO}$ mol$_{Ni+Fe}^{-1}$;. (2) 5.02 mol$_{CO}$ mol$_{Ni+Fe}^{-1}$; (3) 6.28 mol$_{CO}$ mol$_{Ni+Fe}^{-1}$.

accumulated more carbon, as 6.28 mol$_{CO}$ mol$_{Ni+Fe}^{-1}$ was produced after carbon removal, while on 0.7-Fe/Ni and 0-Fe/Ni less carbon was deposited (production of 5.02 and 2.47 mol$_{CO}$ mol$_{Ni+Fe}^{-1}$ respectively). The reference 5Fe sample produced 2.4 mol$_{CO}$ mol$_{Ni+Fe}^{-1}$ (not shown), implying that Fe can be an active site for the methane decomposition reaction.[65]

As the total metal loading increases in the mixed Fe-Ni samples, more carbon is formed. This is in accordance with Shah and co-workers[63] and Baker,[66] who also showed that bimetallic catalysts are more active for methane decomposition than the monometallic catalysts. This implies that the reduced amount of carbon observed in SEM-EDX after methane dry reforming over Fe-promoted catalysts was not due to the alloy formation between Ni and Fe. Rather, another phenomenon is responsible for this observation.

3.6. Time-Resolved in Situ XRD during DRM. To understand the reason for the lower amount of carbon deposited on Fe modified samples under dry reforming reaction conditions, despite the higher amount deposited during CH_4 decomposition, in situ XRD experiments were performed on all studied catalysts. Initially, all samples were reduced during H_2-TPR at 1023 K, at a heating rate of 30 K/min and a flow rate of 1 mL/s 10% H_2/He, in order to form the active Fe-Ni alloy (period 1 in Figure 13). Then, a flow of CH_4 and CO_2 was introduced to the reactor (periods 2−4 in Figure 13), stepwise increasing the CO_2 partial pressure and investigating the effect on alloy decomposition. When the CO_2 partial pressure was 6 times higher than the CH_4 partial pressure, an FeO peak was observed in in situ XRD, implying that Fe was extracted from the alloy. Likely, FeO is formed in the presence of CO_2 even at lower partial pressures but is then not detected by in situ XRD due to its low concentration. Samples with Fe loading higher than 0.7-Fe/Ni exhibited a FeO peak even at higher CH_4/CO_2 ratios.

According to Galvita and co-workers[67] carbon deposition is not favored on iron oxides, in the presence of an oxidizing agent, for temperatures between 1023 and 1173 K. Hence, it is likely that most of the carbon will be formed during dry reforming on the Ni surface. In this mechanism, methane is decomposed over a Ni particle to form hydrogen and carbon. In the presence of CO_2 metallic Fe is segregated from the alloy and FeO_x is formed. Subsequently, oxygen from the FeO_x lattice is transferred to a nearby Ni atom, oxidizing the formed carbon and producing CO. This is in accordance with Galvita and co-workers,[64] who performed reduction/oxidation cycles over Ni/CeO_2-Fe_2O_3. The initial reduction step of the as-prepared catalyst in a gas stream of CH_4+CO_2 resulted in Fe-Ni alloy formation which was stable in an inert environment. After CO_2 oxidation they observed that surface carbon was further oxidized by iron oxide lattice oxygen, since in an inert environment the iron oxide was further reduced to metallic Fe.

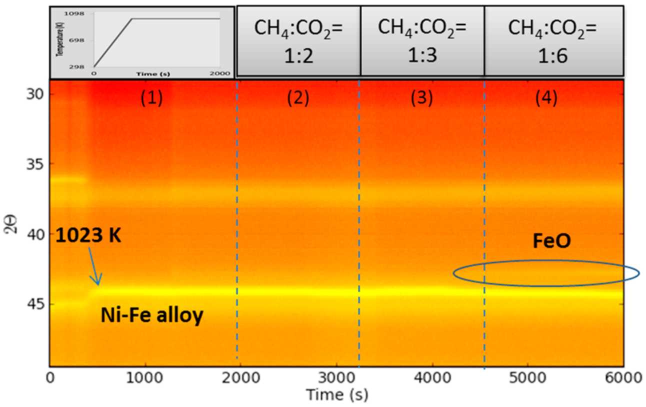

Figure 13. Time-resolved in situ XRD patterns of a 0.7-Fe/Ni sample: (1) Fe-Ni alloy formation in 10% H_2-TPR to 1023 K at a heating rate of 30 K/min; (2−4) methane dry reforming at (2) CH_4/CO_2 = 1/2, (3) CH_4/CO_2 = 1/3, and (4) CH_4/CO_2 = 1/6 at 1023 K and a total pressure of 101.3 kPa.

3.7. Alternate Pulse Experiment. To understand the mechanism for CH_4 and CO_2 activation on Fe-Ni catalysts, an alternate pulse experiment was performed. CO_2 and CH_4 were sequentially pulsed into the reactor at 1023 K over a reduced catalyst, while the outlet flow rate of CO production was measured. Parts A and B of Figure 14 show that CO was produced on the 1.1-Fe/Ni and 5Fe catalysts during the CO_2 pulse. When the values were normalized per mole of Fe, 1.1-Fe/Ni and 5Fe produced 8.4 and 6.1 mol$_{CO}$ mol$_{Fe}^{-1}$, respectively. However, there was no CO production on the 0-Fe/Ni sample during a CO_2 pulse (not shown), which is in accordance with Figure 4A, where it was shown that Ni is not oxidized under a CO_2 flow. Subsequently, He was introduced into the reactor to remove the remaining CO_2. During the subsequent CH_4 pulse, CO was formed only over 1.1-Fe/Ni catalyst (7.3 mol$_{CO}$ mol$_{Fe}^{-1}$), while no CO production was observed over a pure 5Fe sample (Figure 14B), implying that FeO_x is not active for the methane decomposition reaction. The behavior of CO_2 oxidation and CH_4 reduction observed in Figure 14A is consistent with a Mars−van Krevelen (MvK) mechanism.

During the first pulse, Fe is oxidized by CO_2 to form FeO_x and CO is produced. During the reduction step (second pulse) methane is activated and decomposed to carbon and H_2 only on the Ni surface due to the low activity of FeO_x in methane activation (Figure 14B). Lattice oxygen atoms from the surface and bulk of FeO_x are consumed by carbon deposited on nearby Ni. The carbon balance during the CH_4 pulse was calculated, and the estimated carbon remaining on the catalyst surface was 24% of the carbon feed. This can be attributed either to the fact that the amount of pulsed CO_2 was not high enough to remove

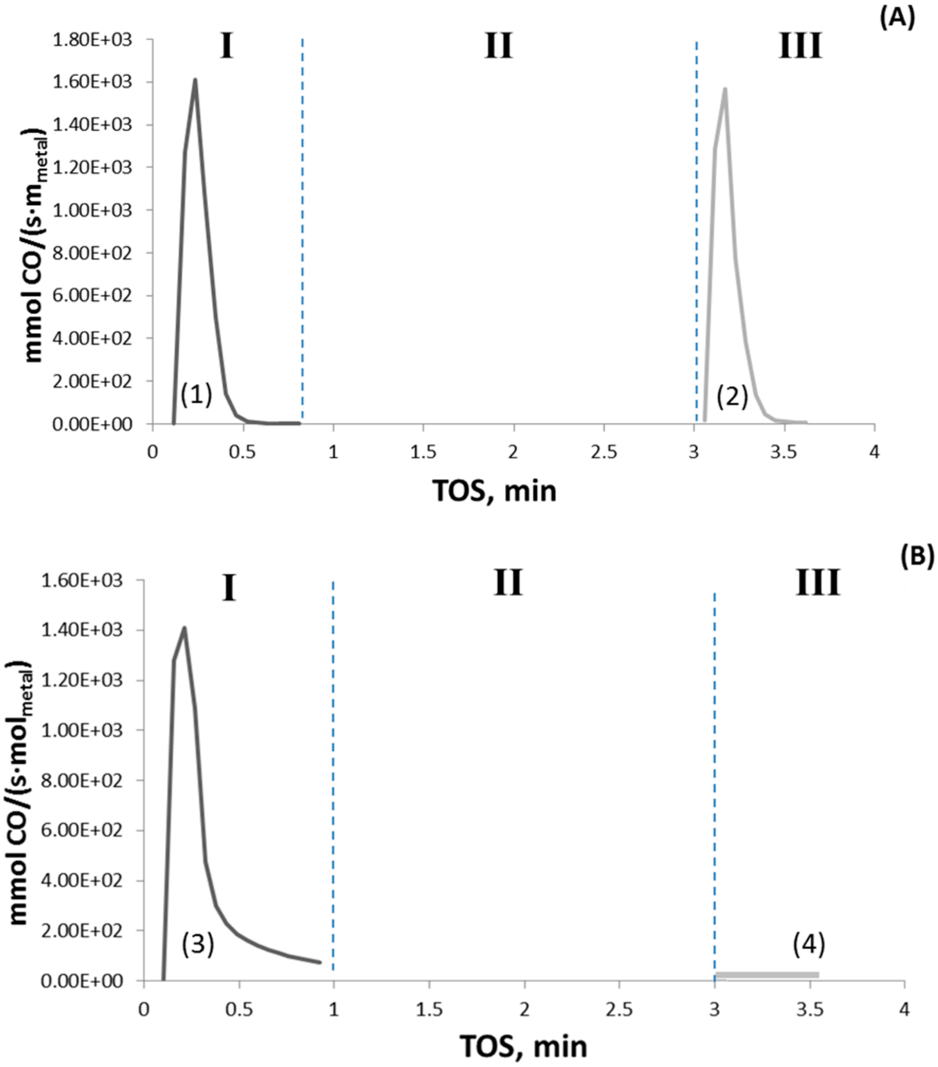

Figure 14. CO production during CO_2 and CH_4 alternate pulse experiment over (A) 1.1-Fe/Ni and (B) 5% Fe. Conditions (1023 K, total pressure of 101.3 kPa): period I, 1 mL/s of CO_2, 1 min; period II, 1 mL/s of He, 2 min; period III, 1 mL/s of CH_4, 1 min. Values of $mol_{CO}\ mol_{metal}^{-1}$ produced: (1) 8.4; (2) 6.1; (3) 7.3; (4) 0.0.

all carbon or to different types or locations of carbon.[68] This carbon can be burnt only by oxygen at temperatures higher than 1023 K.

The opposite sequence of pulses was also investigated (see section 3.5), where the CH_4 pulse was first sent, followed by the CO_2 pulse. CO production was observed for all of the examined samples, during the CO_2 pulse, due to oxidation of the deposited carbon.

In general, a dry reforming reaction is typically accompanied by the simultaneous occurrence of the reverse water-gas shift reaction ($CO_2 + H_2 \Leftrightarrow CO + H_2O$). To study the interaction between the hydrogen, being the product of methane dry reforming, and CO_2, a CO_2 and H_2 alternate pulse experiment was performed using the same volumetric flow rates as in the CH_4/CO_2 alternate pulse experiment. It followed that the reverse water-gas shift reaction over Fe-promoted catalysts proceeds via a simple redox mechanism: CO_2 oxidizes the Fe surface, while H_2 reduces it.

The results obtained from pulse experiments on the catalyst can give us some insights into the major mechanistic aspects of the dry reforming reaction. It is suggested that both methane dry reforming and reverse water-gas shift reactions can proceed via a MvK mechanism over 1.1-Fe/Ni. The constituent formal reactions of methane dry reforming can be described by the equations

$$CH_4 \overset{Ni}{\rightarrow} C_{Ni} + 2H_2 \tag{7}$$

$$Fe + xCO_2 \rightleftarrows FeO_x + xCO \tag{8}$$

$$FeO_x + C_{Ni} \rightleftarrows xCO + Ni + Fe \tag{9}$$

$$FeO_x + H_2 \rightleftarrows Fe + H_2O \tag{10}$$

However, the carbon oxidation from surface oxygen produced by CO_2 dissociation over Ni cannot be excluded.[69] In the Fe-Ni catalytic system, CH_4 is activated by Ni sites and dissociates to H_2 and chemisorbed carbon (eq 7), whereas CO_2 is dissociatively adsorbed on Fe sites, producing surface CO and Fe oxide (eq 8). In contrast to the nonpromoted sample, 0-Fe/Ni, the lattice oxygen from iron oxide participates in the reaction mechanism, oxidizing the carbon deposited on the nearby Ni atoms, thereby forming CO and carbon-free Ni sites (eq 9).[64] The FeO_x lattice oxygen can also react with produced H_2, resulting in H_2O formation (eq 10). Equations 8 and 10 are the steps for the reverse WGS reaction that arises simultaneously with the DRM reaction.

4. CONCLUSIONS

The evolution of the crystallographic structure of bimetallic Fe-Ni/$MgAl_2O_4$ catalysts with varying Ni/Fe ratios was investigated using time-resolved in situ XRD. During H_2-TPR, Fe_2O_3 and NiO were reduced above 973 K to form a Fe-Ni alloy, which constitutes the active phase for the methane dry reforming reaction. This alloy remained stable in a flowing gas stream of CO_2 during reoxidation, until 900 K, but was decomposed to metallic Ni and Fe_3O_4 above this temperature.

The effect of Fe addition to the activity of a Ni/$MgAl_2O_4$ catalyst, under methane dry reforming reaction conditions, was found to depend on the employed Ni/Fe ratio. Activity measurements indicated that 0.7-Fe/Ni presented a high selectivity toward CO and a CO/H_2 ratio close to unity. Furthermore, the implementation of regeneration cycles showed that the catalyst activity can be restored.

Alternate CH_4 and CO_2 pulse experiments and in situ XRD over Fe/$MgAl_2O_4$, Ni/$MgAl_2O_4$, and Fe-Ni/$MgAl_2O_4$ catalysts allowed us to propose a mechanism of methane dry reforming over the Fe-Ni catalysts. The process of dry reforming on Fe-Ni could be described by the Mars−van Krevelen mechanism, where CO_2 oxidizes Fe to FeO_x and CH_4 is activated on Ni sites to form H_2 and surface carbon. The latter was reoxidized by lattice oxygen from FeO_x, producing CO. Lower amounts of accumulated carbon were observed after DRM on Fe-promoted samples in comparison to the pure Ni/$MgAl_2O_4$ sample.

■ AUTHOR INFORMATION

Corresponding Author

*E-mail for V.V.G.: Vladimir.Galvita@UGent.be.

Notes

The authors declare no competing financial interest.

■ ACKNOWLEDGMENTS

This work was supported by the FAST industrialization by Catalyst Research and Development (FASTCARD) project, which is a Large Scale Collaborative Project supported by the European Commission in the 7th Framework Programme (GA no 604277), by the "Long Term Structural Methusalem Funding by the Flemish Government" and the Interuniversity Attraction Poles Programme, IAP7/5, Belgian State-Belgian Science Policy. The authors acknowledge support from Prof. C. Detavernier with the in situ XRD equipment (Department of Solid State Sciences, Ghent University) and from Dr. Vitaliy Bliznuk (Department of Materials Science and Engineering, Ghent University) for the HRTEM measurements.

■ REFERENCES

(1) Littlewood, P.; Xie, X.; Bernicke, M.; Thomas, A.; Schomäcker, R. *Catal. Today* **2015**, *242* (Part A), 111−118.

(2) Pakhare, D.; Schwartz, V.; Abdelsayed, V.; Haynes, D.; Shekhawat, D.; Poston, J.; Spivey, J. *J. Catal.* **2014**, *316*, 78−92.

(3) Luisetto, I.; Tuti, S.; Di Bartolomeo, E. *Int. J. Hydrogen Energy* **2012**, *37*, 15992−15999.

(4) Damyanova, S.; Pawelec, B.; Arishtirova, K.; Fierro, J. L. G. *Int. J. Hydrogen Energy* **2012**, *37*, 15966−15975.

(5) Nematollahi, B.; Rezaei, M.; Khajenoori, M. *Int. J. Hydrogen Energy* **2011**, *36*, 2969−2978.

(6) Rezaei, M.; Alavi, S. M.; Sahebdelfar, S.; Yan, Z.-F. *J. Nat. Gas Chem.* **2006**, *15*, 327−334.

(7) Bradford, M. C. J.; Vannice, M. A. *Catal. Rev.: Sci. Eng.* **1999**, *41*, 1−42.

(8) Guo, J.; Xie, C.; Lee, K.; Guo, N.; Miller, J. T.; Janik, M. J.; Song, C. *ACS Catal.* **2011**, *1*, 574−582.

(9) Sadykov, V. A.; Gubanova, E. L.; Sazonova, N. N.; Pokrovskaya, S. A.; Chumakova, N. A.; Mezentseva, N. V.; Bobin, A. S.; Gulyaev, R. V.; Ishchenko, A. V.; Krieger, T. A.; Mirodatos, C. *Catal. Today* **2011**, *171*, 140−149.

(10) Tsipouriari, V. A.; Efstathiou, A. M.; Verykios, X. E. *J. Catal.* **1996**, *161*, 31−42.

(11) Efstathiou, A. M.; Kladi, A.; Tsipouriari, V. A.; Verykios, X. E. *J. Catal.* **1996**, *158*, 64−75.

(12) Ashok, J.; Kawi, S. *Int. J. Hydrogen Energy* **2013**, *38*, 13938−13949.

(13) Ashok, J.; Subrahmanyam, M.; Venugopal, A. *Int. J. Hydrogen Energy* **2008**, *33*, 2704−2713.

(14) Ashok, J.; Kawi, S. *ACS Catal.* **2013**, *4*, 289−301.

(15) Nakamura, K.; Miyazawa, T.; Sakurai, T.; Miyao, T.; Naito, S.; Begum, N.; Kunimori, K.; Tomishige, K. *Appl. Catal., B* **2009**, *86*, 36−44.

(16) Alipour, Z.; Rezaei, M.; Meshkani, F. *J. Ind. Eng. Chem.* **2014**, *20*, 2858−2863.

(17) Swaan, H. M.; Kroll, V. C. H.; Martin, G. A.; Mirodatos, C. *Catal. Today* **1994**, *21*, 571−578.

(18) Bobin, A. S.; Sadykov, V. A.; Rogov, V. A.; Mezentseva, N. V.; Alikina, G. M.; Sadovskaya, E. M.; Glazneva, T. S.; Sazonova, N. N.; Smirnova, M. Y.; Veniaminov, S. A.; Mirodatos, C.; Galvita, V.; Marin, G. B. *Top. Catal.* **2013**, *56*, 958−968.

(19) Xu, L.; Song, H.; Chou, L. *Appl. Catal., B* **2011**, *108−109*, 177−190.

(20) Xu, Z.; Li, Y.; Zhang, J.; Chang, L.; Zhou, R.; Duan, Z. *Appl. Catal., A* **2001**, *210*, 45−53.

(21) Kang, K.-M.; Kim, H.-W.; Shim, I.-W.; Kwak, H.-Y. *Fuel Process. Technol.* **2011**, *92*, 1236−1243.

(22) Arandiyan, H.; Li, J.; Ma, L.; Hashemnejad, S. M.; Mirzaei, M. Z.; Chen, J.; Chang, H.; Liu, C.; Wang, C.; Chen, L. *J. Ind. Eng. Chem.* **2012**, *18*, 2103−2114.

(23) He, S.; Wu, H.; Yu, W.; Mo, L.; Lou, H.; Zheng, X. *Int. J. Hydrogen Energy* **2009**, *34*, 839−843.

(24) Zhang, Q.-H.; Li, Y.; Xu, B.-Q. *Catal. Today* **2004**, *98*, 601−605.

(25) Sokolov, S.; Kondratenko, E. V.; Pohl, M.-M.; Rodemerck, U. *Int. J. Hydrogen Energy* **2013**, *38*, 16121−16132.

(26) Xie, X.; Otremba, T.; Littlewood, P.; Schomäcker, R.; Thomas, A. *ACS Catal.* **2012**, *3*, 224−229.

(27) Nair, M. M.; Kaliaguine, S.; Kleitz, F. *ACS Catal.* **2014**, *4*, 3837−3846.

(28) Gal'vita, V. V.; Belyaev, V. D.; Parmon, V. N.; Sobyanin, V. A. *Catal. Lett.* **1996**, *39*, 209−211.

(29) Kroll, V. C. H.; Swaan, H. M.; Lacombe, S.; Mirodatos, C. *J. Catal.* **1996**, *164*, 387−398.

(30) Zhang, Z.; Verykios, X. E. *Appl. Catal., A* **1996**, *138*, 109−133.

(31) Pakhare, D.; Spivey, J. *Chem. Soc. Rev.* **2014**, *43*, 7813−7837.

(32) Slagtern, A.; Schuurman, Y.; Leclercq, C.; Verykios, X.; Mirodatos, C. *J. Catal.* **1997**, *172*, 118−126.

(33) Bobin, A. S.; Sadykov, V. A.; Rogov, V. A.; Mezentseva, N. V.; Alikina, G. M.; Sadovskaya, E. M.; Glazneva, T. S.; Sazonova, N. N.; Smirnova, M. Y.; Veniaminov, S. A.; Mirodatos, C.; Galvita, V.; Marin, G. B. *Top. Catal.* **2013**, *56*, 958−968.

(34) Guo, J.; Lou, H.; Zhao, H.; Chai, D.; Zheng, X. *Appl. Catal., A* **2004**, *273*, 75−82.

(35) Penkova, A.; Bobadilla, L.; Ivanova, S.; Domínguez, M. I.; Romero-Sarria, F.; Roger, A. C.; Centeno, M. A.; Odriozola, J. A. *Appl. Catal., A* **2011**, *392*, 184−191.

(36) Hadian, N.; Rezaei, M.; Mosayebi, Z.; Meshkani, F. *J. Nat. Gas Chem.* **2012**, *21*, 200−206.

(37) Guo, J.; Lou, H.; Zhao, H.; Wang, X.; Zheng, X. *Mater. Lett.* **2004**, *58*, 1920−1923.

(38) Alvar, E. N.; Rezaei, M. *Scr. Mater.* **2009**, *61*, 212−215.

DOI: 10.1021/acscatal.5b00357
ACS Catal. 2015, 5, 3028−3039

(39) Kambolis, A.; Matralis, H.; Trovarelli, A.; Papadopoulou, C. *Appl. Catal., A* **2010**, *377*, 16−26.
(40) Miyazawa, T.; Kimura, T.; Nishikawa, J.; Kado, S.; Kunimori, K.; Tomishige, K. *Catal. Today* **2006**, *115*, 254−262.
(41) Koike, M.; Ishikawa, C.; Li, D.; Wang, L.; Nakagawa, Y.; Tomishige, K. *Fuel* **2013**, *103*, 122−129.
(42) Wang, L.; Li, D.; Koike, M.; Koso, S.; Nakagawa, Y.; Xu, Y.; Tomishige, K. *Appl. Catal., A* **2011**, *392*, 248−255.
(43) Li, D.; Atake, I.; Shishido, T.; Oumi, Y.; Sano, T.; Takehira, K. *J. Catal.* **2007**, *250*, 299−312.
(44) Nagaoka, K.; Jentys, A.; Lercher, J. A. *J. Catal.* **2005**, *229*, 185−196.
(45) Crisafulli, C.; Scirè, S.; Maggiore, R.; Minicò, S.; Galvagno, S. *Catal. Lett.* **1999**, *59*, 21−26.
(46) Li, D.; Nakagawa, Y.; Tomishige, K. *Appl. Catal., A* **2011**, *408*, 1−24.
(47) Wang, L.; Li, D.; Koike, M.; Watanabe, H.; Xu, Y.; Nakagawa, Y.; Tomishige, K. *Fuel* **2013**, *112*, 654−661.
(48) Tian, D.; Liu, Z.; Li, D.; Shi, H.; Pan, W.; Cheng, Y. *Fuel* **2013**, *104*, 224−229.
(49) Haber, J.; Block, J. H.; Delmon, B. *Pure Appl. Chem.* **1995**, DOI: 10.1351/pac199567081257.
(50) Scherrer, P. *Nachr. Ges. Wiss. Göttingen* **1918**, *2*, 98−100.
(51) Niemantsverdiet, W. J. *Spectroscopy in Catalysis*; Wiley-VCH: Weinheim, Germany, 2007
(52) Olsbye, U.; Moen, O.; Slagtern, Å.; Dahl, I. M. *Appl. Catal., A* **2002**, *228*, 289−303.
(53) Fromen, G. F.; Bischoff, K. *Chemical Reactor Analysis and Design*; Wiley: New York, 1990.
(54) Mears, D. E. *J. Catal.* **1971**, *20*, 127−131.
(55) Galvita, V. V.; Poelman, H.; Marin, G. B. *J. Power Sources* **2015**, *286*, 362−370.
(56) Kustov, A. L.; Frey, A. M.; Larsen, K. E.; Johannessen, T.; Nørskov, J. K.; Christensen, C. H. *Appl. Catal., A* **2007**, *320*, 98−104.
(57) *Handbook of Binary Alloy Phase Diagrams*; ASM International: Materials Park, OH, 1996
(58) Simonsen, S. B.; Chakraborty, D.; Chorkendorff, I.; Dahl, S. *Appl. Catal., A* **2012**, *447*−*448*, 22−31.
(59) Gheisari, K.; Javadpour, S.; Oh, J. T.; Ghaffari, M. *J. Alloys Compd.* **2009**, *472*, 416−420.
(60) Galvita, V. V.; Poelman, H.; Bliznuk, V.; Detavernier, C.; Marin, G. B. *Ind. Eng. Chem. Res.* **2013**, *52*, 8416−8426.
(61) Goodman, D. W. *Catal. Today* **1992**, *12*, 189−199.
(62) Beebe, T. P.; Goodman, D. W.; Kay, B. D.; Yates, J. T. *J. Chem. Phys.* **1987**, *87*, 2305−2315.
(63) Shah, N.; Panjala, D.; Huffman, G. P. *Energy Fuels* **2001**, *15*, 1528−1534.
(64) Galvita, V. V.; Poelman, H.; Detavernier, C.; Marin, G. B. *Appl. Catal., B* **2015**, *164*, 184−191.
(65) Alexiadis, V. I.; Boukos, N.; Verykios, X. E. *Mater. Chem. Phys.* **2011**, *128*, 96−108.
(66) Baker, R. T. K. *Prepr. Pap., Am. Chem. Soc., Div. Fuel Chem.* **1996**, *41*, 521−524.
(67) Galvita, V.; Schröder, T.; Munder, B.; Sundmacher, K. *Int. J. Hydrogen Energy* **2008**, *33*, 1354−1360.
(68) Horváth, A.; Stefler, G.; Geszti, O.; Kienneman, A.; Pietraszek, A.; Guczi, L. *Catal. Today* **2011**, *169*, 102−111.
(69) Wei, J.; Iglesia, E. *J. Catal.* **2004**, *224*, 370−383.